A&A 668, A149 (2022)
https://doi.org/10.1051/0004-6361/202243464

Astronomy & Astrophysics

A prototype of a microlensed hyperspectral imager for solar observations

M. van Noort[1], J. Bischoff[1], A. Kramer[1], S. K. Solanki[1,2], and D. Kiselman[3]

[1] Max Planck Institute for Solar System Research, Justus-von-Liebig-Weg 3, 37077 Göttingen, Germany
e-mail: vannoort@mps.mpg.de
[2] School of Space Research, Kyung Hee University, Yongin, Gyeonggi 446-701, Republic of Korea
[3] Institute for Solar Physics, Department of Astronomy, Stockholm University, 106 91 Stockholm, Sweden

Received 3 March 2022 / Accepted 20 October 2022

ABSTRACT

Context. When spectropolarimetric data are recorded at high spatial, spectral, and temporal resolution, the quality of the data is generally limited by the signal-to-noise ratio.
Aims. We present a prototype of an integral field spectrograph for solar observations. This prototype overcomes the limitations of traditional solar instrumentation and captures the spectral information for all points in a given field of view without scanning, in order to optimize the efficiency and to minimize spectral and spatial crosstalk.
Methods. The prototype was executed as a plug-in for the TRIPPEL spectrograph at the Swedish 1-meter Solar Telescope (SST) and uses an array of microlenses to shrink each image element, so that dark space is created in between. The light is then dispersed in this space, allowing for the independent detection of each spatio-spectral image element on a 2D detector.
Results. The prototype was built and installed at the SST, yielding several good-quality data sets. These data sets were used to determine the imaging performance and efficiency of the prototype.
Conclusions. Although the instrument required high-accuracy optics, the transparency of the prototype was found to be about 25%, and the straylight properties were found to be typical for spectrographic instruments.

Key words. instrumentation: spectrographs – instrumentation: polarimeters – techniques: imaging spectroscopy – methods: observational

1. Introduction

The light coming to us from the Sun is characterized by its intensity and polarization state, and it can be described by a set of four Stokes parameters as a function of space, time, and wavelength. The information space of each Stokes parameter thus has four dimensions, all of which encode important information concerning the conditions that prevail at the location from which the light has originated at the time of the observation. To preserve this information in observational data, it is critical that it is registered as independently as possible by the instrument used in the observation, so as to maximize the information about the physical conditions in the solar atmosphere that can be extracted from the data.

This realization is not new, and it has led to the development of many different types of instruments for solar observations, so-called hyperspectral imagers, most of which aim to obtain the hypercube of information by sequential sampling, using a 2D detector array to sample the data. When we consider that the time dimension is special and must be sampled independently, this still leaves one dimension to be sampled sequentially, which is typically accomplished by multiplexing in time.

If the multiplexed dimension is the wavelength, the instrument is a narrowband tunable filter, such as Lyot or Fabry–Pérot filters. While the former have enjoyed great popularity in the past (e.g., the Universal Birefringent Filter (UBF, Beckers et al. 1975), the Solar Optical Universal Polarimeter (SOUP, Title & Rosenberg 1981), or the Hinode Narrowband Filter Imager (NFI, Shimizu 2004)), their low transmission and low tuning speed have caused most of them to be replaced by larger, faster, and more efficient Fabry–Pérot based filters (e.g., the Telecentric Etalon SOlar Spectrometer (TESOS, Kentischer et al. 1998), the Interferometric BIdimensional Spectrometer (IBIS, Cavallini 2006), the CRIsp Solar Polarimeter (CRISP, Scharmer 2006), the CHROMospheric Imaging Spectrograph (CHROMIS, Scharmer 2017), the GREGOR Fabry–Pérot Interferometer (GFPI, Puschmann et al. 2012), or the Near-InfraRed Imaging Spectrograph (NIRIS, Cao et al. 2012)). Filters like these have provided the bulk of solar observations over the past two decades or so, but their limitations are still considerable. Although a typical tunable Fabry–Pérot filter used for solar observations is really quite fast and can change the selected wavelength in 100 ms or less, not more than 10-20 wavelength positions can be selected before the time sampling of the data cube becomes problematic when we consider the time it takes to collect enough light for an image with a sufficiently high signal-to-noise ratio (S/N) to allow for sensitive polarimetry. It is thus not the speed of the filter that limits performance, but the sequential nature of the data acquisition.

If the instrument is a long-slit spectrograph (Hinode Spectro-Polarimeter (SP, Lites et al. 2001), the GREGOR Imaging Spectrograph (GRIS, Collados et al. 2012), the TRI-Port Polarimetric Echelle-Littrow (TRIPPEL, Kiselman et al. 2011) spectrograph, or the Fast Imaging Solar Spectrograph (FISS, Chae et al. 2013), to name just a few), the multiplexed dimension is spatial, and the wavelengths are separated by means of a dispersive element. Although many wavelengths can be observed simultaneously, one spatial dimension must be masked by using a slit, which

now needs to be scanned in time. It is obvious that the same problem results as for filtergraphs, and only a narrow region can be scanned before the temporal sampling becomes questionable.

Although unlike the Sun, many night-time objects are too intrinsically large and poorly resolved to show rapid time evolution, a similar problem still exists in night time observations. There, the collection of spectral information for an individual star in a field of view (FOV) requires the telescope to center on that star and record the spectrum. Recording a spectrum for each star in the FOV in this way, or alternatively, scanning an entire spectrum with a narrowband filter, thus requires too much time.

When this problem was identified by the night-time astronomical community many decades ago, a number of so-called integral field solutions were proposed to fit all three dimensions of the coveted data cube onto a 2D detector. Over the decades, all of these have been used extensively and with great success in observations on night-time telescopes (e.g., the Traitement Intégral des Galaxies par l'Étude de leur Raies (TIGER, Bacon et al. 1995), the SPectrometer for Infrared Faint Field Imaging (SPIFFI, Tecza et al. 2000), the Spectroscopic Areal Unit for Research on Optical Nebulae (SAURON, Bacon et al. 2001), the Multi Unit Spectroscopic Explorer (MUSE, Henault et al. 2003), the OSIRIS integral field spectrograph (Larkin et al. 2006), the Gemini Planet Imager (GPI, Macintosh et al. 2006), the Coronagraphic High Angular Resolution Imaging Spectrograph (CHARIS, Groff et al. 2014), and the Spectro-Polarimetic High contrast imager for Exoplanets REsearch (SPHERE, Beuzit et al. 2019)). Most of these instruments are not designed to have a very high spectral resolution (<4000) because it is challenging to detect and store the large amount of information that is generated by such instruments, and many of the night-time applications favor spectral range over spectral resolution.

Solar observations differ substantially from night-time observations in that the Sun is currently the only star of its type that can be spatially resolved. The relatively modest differences in the physical properties between these highly resolved structures typically result in subtle differences in the emitted spectra, which require a high spectral resolution to resolve. This imposes quite different requirements on a solar integral field spectrograph because it must not only have a high spectral resolution, it also needs to preserve the spatial resolution, so that it can operate at or near the diffraction limit of the telescope that is used for the observations. In addition, because the Sun is an extended light source, it must have very low straylight properties and a very high optical stability, so that accurate differential photometric measurements, suitable for measuring the polarimetric state of the light, can be obtained over prolonged periods of time. Finally, it must be able to deliver data at a high cadence, so that time-dependent changes in the structures on the solar surface can be adequately resolved and tracked.

One such solution, pioneered by Mein & Blondel (1972), is the Multichannel Subtractive Double Pass (MSDP) spectrograph, which is able to produce an array of strictly simultaneous, spatially separated narrowband images. However, the direct coupling between the FOV and the spectral bandwidth of the images imposes significant limits on the spectral resolution that can be achieved. Moreover, the intrinsic drift of the central wavelength of the passband across each image interferes with image restoration techniques and complicates the interpretation of the data. Consequently, these types of instruments have not seen extensive use in the recent past.

The past two decades have seen a significant increase in the number of attempts to build an instrument without these drawbacks, using a microlens array (MLA; Suematsu et al. 1999), fiber arrays (the SpectroPolarimetric Imager for the Energetic Sun (SPIES, Lin 2012), birefringent fiber optic image slicer (BiFOIS, Schad et al. 2014), and the Fiber Arrayed Solar Optical Telescope (FASOT, Qu et al. 2017)), and optical image slicers (Solar-C SP (Suematsu et al. 2017) and the Multi-Slit Image slicer based on collimator-Camera (MuSICa, Dominguez-Tagle et al. 2018)). These attempts have shown that constructing an instrument that combines good stability, high spectral resolution, and low straylight properties is very challenging.

In this paper, we present a modified optical concept for a microlens-based integral field spectrograph for solar applications. The properties of the microlenses are analyzed in detail, resulting in the design of an inherently stable, two microlens micro-optical reimaging system with good optical properties. A prototype of this instrument was then constructed and tested on the Swedish 1-meter Solar Telescope (SST; Scharmer et al. 2003), and an evaluation of the instrumental properties is presented here.

2. Microlensed hyperspectral imaging

The primary goal of any integral field spectrograph is to simultaneously register the spatial and spectral structure of the light that it receives. This is usually done by reorganizing the light in a 2D plane such that it can be dispersed by a spectrograph grating, without causing any of the spectral information to overlap. This must be accomplished without compromising the spectral and spatial resolution, and in a way that guarantees stable instrument properties.

Of the various possible solutions to the integral field problem, the microlensed hyperspectral imager (MiHI) concept represents the smallest modification that can be made to a long-slit spectrograph that gives it integral field capabilities. The basic concept, illustrated in Fig. 1, consists of an MLA that sample the telescope focal plane and scale each of the image elements down to a fraction of their size. The array of point sources created by the MLA is then fed into a spectrograph, and dispersed. To prevent overlap of the spectra, the dispersion direction is tilted with respect to the grid direction of the MLA, and a narrowband prefilter is placed in the beam.

The simplicity, however, is only apparent, and a previous attempt to construct such an instrument for solar observations (Suematsu et al. 1999) did not result in the publication of data with a high spatial and spectral resolution. If an instrument that can compete with existing solar instrumentation is to be constructed, any problems that were encountered will need to be understood and addressed.

2.1. Instrument requirements

The introduction of direct electronic imaging devices in the 1980s has transformed ground-based solar observations, triggering the development of numerical methods to restore raw solar images, degraded by distortions and optical aberrations from the Earth's atmosphere and instrumental effects, to their original undegraded state. These so-called image restoration techniques, by now an integral part of most solar data reduction pipelines, typically operate on the data in Fourier space, and thus require the data to be critically sampled, that is, the data must be sampled with a minimum of two samples per wave of the highest signal frequency that is present in the data (Nyquist 1928; Shannon 1949). It is therefore essential that the telescope focal plane is sampled critically by the prototype.

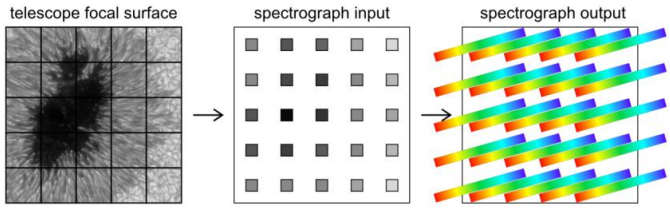

Fig. 1. Working principle of a microlens-based integral field spectrograph. The focal plane (*left*) is sampled with microlenses. The image elements are then demagnified (*center*) and are finally dispersed (*right*). The dispersion direction of the spectrograph is tilted with respect to the grid direction of the MLA to avoid overlap of the spectra.

The current state of the art in solar instrumentation is that for a critically sampled focal plane, an S/N of approximately 10^3 can be achieved at a spectral resolving power of 10^5 in approximately 1s. With a fast, tunable filter at that resolving power, a single spectral line can be sampled with approximately 10 points, taking approximately 10 s. We consider these values to represent the minimum requirements for an integral field spectrograph to be of competitive value.

Because we aim to build a MiHI prototype, it makes sense to restrict the spectral range to a single spectral window. This is both easy to work with in a laboratory environment and has been well studied in the past using other instruments, so that a cross comparison of the results can be made. The window was chosen around 6302 Å because the solar spectrum there contains two magnetically sensitive Fe I lines that were also selected for the spectropolarimeter (Lites et al. 2001) on board the Hinode space telescope (Kosugi et al. 2007). Additionally, the spectrum observed from the ground contains several telluric O_2 lines that provide a convenient wavelength reference for the spectra, and the wavelength of 6302 Å is very close to a well-known Ne line at 633 nm that is used in many commercially available He-Ne lasers. This line can be readily used for alignment and calibration purposes.

From the extensive work done with the Fe I line pair at 6301.5 and 6302.5 Å using Hinode SP data (e.g., Hinode Review Team et al. 2019), it can be concluded that a spectral resolution of 2×10^5 is sufficient to capture most of the relevant features in the solar spectrum at a spatial resolution of 0.26″. At the higher spatial resolution that can be obtained with the best ground-based solar telescopes at this wavelength, less spatial averaging of spectral features leads to more complex line profiles, so that the required spectral resolution is likely to be higher as well. We thus aim for a spectral resolution $R > 2 \times 10^5$, with a spectral range at least as wide as that of the Hinode SP, while critically sampling the focal plane at the diffraction limit of a 1m telescope.

2.2. Microlens design

To understand better why previous attempts to build such an instrument did not produce data of high quality, we made an attempt to model the instrument numerically. The key element to model is clearly the MLA that is used to reduce the size of the original image elements.

2.2.1. Numerical modeling

Because the dimensions of the micro-optical elements in a MLA are somewhere between the domain of photonic structures and that of classical optics, the modeling of a microlens system is not accomplished easily using existing tools. Although photonic modeling tools are in principle able to deal properly with the very small scales, they are designed specifically to handle time-dependent problems. Moreover, because the optical elements are large compared to the wavelength of the light and these methods require the light waves to be sampled accurately to return accurate results, the computational grid needs to be very large and is therefore very demanding computationally.

Considering the light propagating through the MLA to be stationary, however, allows for the use of Huygens' principle (Huygens 1690). In this formalism, the electric field amplitude and phase in the target plane at $z' = z$ are calculated by regarding each point in the source plane at $z' = 0$ to be a radiating point source, s, with known phase and amplitude, E_s. We can calculate the amplitude and phase of the electric field in a target plane by integration over the contributions from all points in the source plane, using

$$E_o(x, y, z) = \frac{z}{i\lambda} \int \int E_s(x', y', 0) \frac{1}{r^2} e^{\frac{-2i\pi r}{\lambda}} \mathrm{d}x' \mathrm{d}y', \tag{1}$$

where $r = \sqrt{(x - x')^2 + (y - y')^2 + z^2}$ is the radial distance from each point in the source plane to the point (x, y, z) in the target plane.

In the regime where the Fresnel condition

$$\left[(x - x')^2 + (y - y')^2\right] \ll z\lambda$$

is satisfied, the second-order terms in the exponent can be neglected, and the integral can be conveniently approximated by a convolution, which leads to the well-known transfer function formalism. Unfortunately, with estimates of the probable dimensions of the microlenses needed for the prototype, this expression is already close to invalid for calculating the contribution of one microlens of the array to the focal plane image at the position of the neighboring microlens, which is necessary to determine the pixel-to-pixel crosstalk.

To ensure accurate results, Eq. (1) was therefore evaluated numerically on a high-density grid, without any further mathematical approximations. While this is a simple task on a modern CPU, the scaling with the number of points is not advantageous and leads to a natural limit of about 1000×1000 grid points in the source and the target planes used in the calculations. The accuracy of the results was confirmed by verifying the robustness of the results using a reduced grid density. The source code of the computer program we used to carry out the calculations presented here is available as part of an online archive of scripts and codes[1].

2.2.2. Optical concept

The evaluation of the beam properties by direct propagation for various microlens sizes reveals that the beam properties of the light leaving the MLA are not related to the optical configuration before the MLA, but rather are set by the physical size of the MLA relative to the wavelength of the light. The requirement of critical sampling of the focal plane of the telescope indirectly implies that the diffraction properties of the microlenses result in a beam F-ratio of the outgoing beam that is approximately half that of the incoming beam, independent of the plate scale of the focal plane. It is therefore the diffraction limit of the MLA that determines the F-ratio of the beam emerging from the MLA,

[1] https://doi.org/10.5281/zenodo.7071196

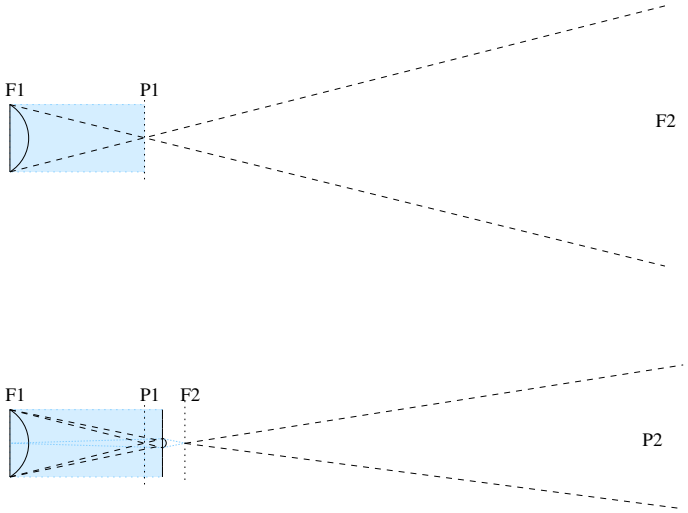

Fig. 2. Two optical concepts for a microlens-based pixel demagnifier. Light travels *from left to right*, $F1$ is the primary telescope focus. *Top panel:* focal plane ($F1$), sampled with microlenses. It reimages the pupil onto a pinhole. The pinhole then reimages $F1$ onto the grating (in $F2$). *Bottom panel:* focal plane sampled with microlenses, reimaging the pupil in $P1$. $F1$ is reimaged with a given demagnification factor in $F2$, while the pupil is reimaged onto the grating (in $P2$).

and this must not be lower than the lowest F-ratio that the spectrograph that receives the light can accommodate. Otherwise, a significant fraction of the light will not be transmitted by the spectrograph.

After being transformed into an array of point sources by the microlenses of the MLA, however, propagation of the light to the grating reveals a more fundamental problem with the MLA. Consider the optical configuration illustrated in the top panel of Fig. 2. Even though the F-ratio of the original telescope beam is not preserved by the microlenses as the beam passes through them, the distribution of light across the microlenses in F_1 is preserved. The demagnified pupil images in P_1 that are produced in the focal plane of the MLA behave effectively like pinholes in an array of camera obscuras, regardless of whether physical pinholes are really present there. These pinhole cameras reimage any image structure that may be present in F_1 onto the grating in F_2. Clearly, if the image has high contrast, this can lead to gradients in the illumination of the grating, causing a significantly reduced performance of the spectrograph and an undesirable, scene-dependent spectral resolution.

To address this issue, a second lens must be inserted between the spectrograph and each image element, imaging not F_1, but P_1 onto the grating instead, as shown in the bottom panel of Fig. 2. This solution corresponds to the so-called BIGRE solution (Antichi et al. 2009), which was developed not to optimize the spectral performance, but to optimize the straylight performance of exoplanet discovery instruments, such as SPHERE (Beuzit et al. 2019). This double microlens design must be proportioned such that the image entering the first lens is reimaged behind the second microlens, and at the same time, P_1 is imaged onto the grating. This is exactly the case when the second lens is placed at approximately its own focal length behind P_1. The image formed in F_2 is scaled by the ratio of the focal lengths of the two microlenses and can be chosen freely, as required by the targeted instrument properties.

The double-lens concept was elaborately studied using the modeling method described in Sect. 2.2.1, revealing a number of interesting properties that were key to the final design requirements.

The image scale of the telescope focal plane is appropriate to be sampled critically with CCD pixels with a pixel size of about 10 µm. To sample this with microlenses that are M times larger, the image scale in F1 must be a factor M larger than in the telescope focal plane, which also increases the F ratio of the beam in $F1$ by a factor M. After the MLA reduces the image scale within each image element by a factor N, where M is usually not very different from N, the size of the image elements is returned approximately to what it was in the telescope focal plane, which should naively also return the F ratio of the beam to approximately that of the telescope beam. However, diffraction on the apertures of the MLA degrades the geometric F ratio of the beam (marked by the vertical blue line in Fig. 3) by a factor of approximately 1.5 (marked by the vertical red line in Fig. 3), which will need to be taken into account when considering the design of the spectrograph.

That diffraction effects dominate the microlens transmission properties implies that a significant fraction of the light in $P1$ is contained in a multitude of diffraction features surrounding a central maximum. Unfortunately, including these diffraction features in addition to the central maximum increases the total transmission only very slowly. This is shown by the blue curve in Fig. 3, which shows the fraction of the transmitted light as a function of the grating size for a spectrograph with an effective focal length of 1500 mm. Clearly, when the central maximum of the diffraction pattern is covered by the grating, the ensquared energy continues to grow only very slowly, suggesting that a grating that only covers the central maximum is probably the best trade-off between grating size and instrument transmission.

Any light that is not reflected by the grating has the potential of being scattered. It therefore makes sense to remove as much of the remaining part of the diffraction pattern as possible with a mask with an appropriately dimensioned pupil stop, thereby improving the overall straylight properties of the instrument. Because this pupil stop itself is also an aperture and will generate its own diffraction pattern in addition to the existing one, numerical experiments were carried out to determine the optimal location and shape of it to minimize the residual diffraction.

For a configuration with a regular grid of square microlenses, the optimal shape for the aperture was determined to be also square, but rotated 45° about the optical axis of the microlens system. This shape has a larger aperture in the direction of maximum diffraction by the microlenses than in the direction of minimum diffraction. A fairly uniform angular distribution of the diffraction effects in the emerging beam can therefore be obtained.

Although $P1$ is the natural place to locate such a mask, numerical modeling showed that placing the mask in the location of the second lens instead did not significantly reduce the effect of it. Fig. 3 was computed from a model that included a 70 µm square mask that was placed at the location of the second microlens and rotated by 45° about the optical axis. It shows that approximately 82% of all the light that enters the front side of the MLA is contained in the primary maximum. This can be captured using a grating that has a size projected onto the pupil plane of the spectrograph of approximately 140×140 mm.

The minimum F ratio of the beam emerging from the MLA can be readily calculated by considering the diffraction of light on an aperture of size d, where d is taken to be the MLA pitch. For the diffraction of waves with a wavelength λ on an aperture with diameter $d \gg \lambda$, classic wave theory predicts an angular separation θ between the center of the central maximum and the

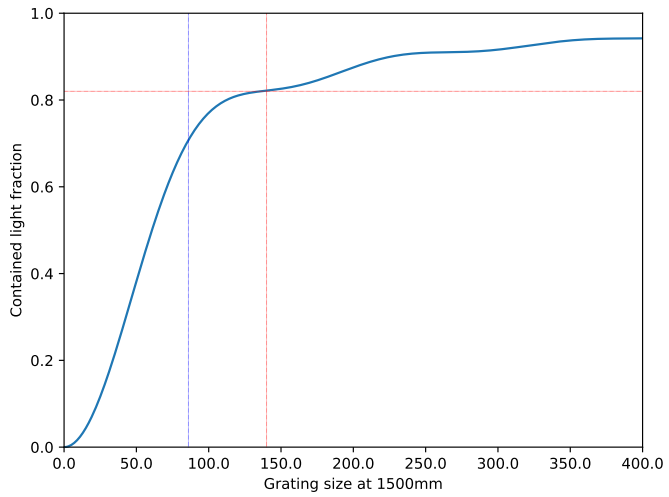

Fig. 3. Fraction of transmitted light as a function of the grating size of a spectrograph with an effective focal length of 1500 mm, calculated using the method from Sect. 2.2.1 for the double-microlens design, with a pitch of 325 µm at a wavelength of 630 nm for $N \approx 18$. The center of the plateau, marked by the horizontal and vertical red lines, corresponds to the grating for which the entire central maximum of the diffraction dominated pupil, containing 82% of the input light, is reflected. The vertical blue line marks the size of the scaled and reimaged telescope pupil.

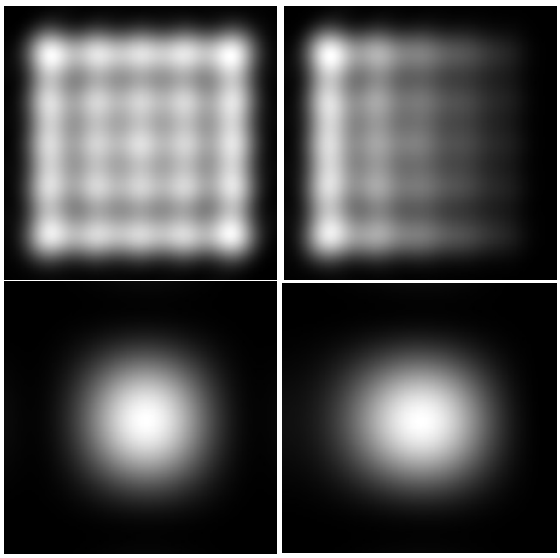

Fig. 4. Calculated response of the double-lens MLA to image contrast. *Top left:* reimaged image element in $F2$ with zero contrast. *Bottom left:* grating illumination at zero contrast. *Top right:* reimaged image element in $F2$ with maximum linear intensity gradient. *Bottom right:* grating illumination for the image element with a maximum linear intensity gradient.

first diffraction minimum of $\theta = 1.22\frac{\lambda}{d}$. We define the F ratio of the beam as the ratio of the diameter of the area covered by the primary maximum, and the distance. Because the double-microlens system is designed to reduce the image scale by a factor N, the F ratio is also decreased by a factor N, resulting in a beam emerging from the MLA that is characterized by

$$F = \frac{d}{2.44\lambda N}. \tag{2}$$

Furthermore, the illumination of the grating is apodized by the diffraction pattern, leading to a change in the optical performance of the spectrograph. The diffraction pattern produced by this apodized pupil has a strongly suppressed diffraction pattern, which is highly beneficial for the straylight properties of the instrument, but at the price of a central maximum that is approximately twice as wide as that produced by an unapodized pupil of the same size.

The vertical dashed red line in Fig. 3 indicates the location of the first minimum in the diffraction pattern, corresponding to the F ratio as defined above. The horizontal character of the curve near this line suggests that using this F ratio for the design of the spectrograph would be underusing the grating near the edges, where the intensity approaches zero rather slowly. For this reason, the real F ratio of the beam can be taken to be somewhat larger, with a minimal loss of light, which has the added advantage that the pupil is less apodized, yielding a better optical performance of the instrument. The exact optimum values for the F ratio and imaging properties of the beam depend primarily on the MLA pitch and the spectrograph properties, and they must be optimized numerically.

The elimination of the influence of image structure on the grating illumination was found to be effective. Figure 4 shows the response of the beam properties to the maximum possible intensity contrast in an element of a critically sampled image (i.e., from 0 to 1 in a linear fashion). The intensity contrast is clearly visible in the image of the scaled image element in $F2$ (top right panel), but this has only a minor effect on the illumination of the grating (bottom right panel) as compared to the uniformly illuminated case (left panels). The small elongation that is visible in the bottom right panel is caused by additional diffraction induced limitations, that is, by the partial illumination of the first microlens in the system. If the spectrograph is able to capture the extended parts of this illumination, a slight enhancement of the optical performance could result, yielding a corresponding small enhancement of the spectral resolution. This effect appears to be rather small, but it could be looked for in a thorough evaluation of such an instrument with real data.

One less positive consequence of the double lens design is the very strong response of the position of the pupil on the grating to relative lateral displacements of the first and second microlenses in the arrays. Because the focal length of the secondary lenses in the MLA is very short, any decenter of these lenses with respect to those in the primary array will be amplified by the factor by which the pupil is enlarged. To reach high spectral resolution, this factor typically needs to be around 10^4, implying that for each micrometer decenter between the lenses on the front and the backsides of the MLA, the pupil will be displaced by 10 mm on the grating.

2.3. Spectral crosstalk

Because no imaging system is able to perfectly image a point in the object plane to a point in the image plane, it is inevitable that a fraction of the light from one image element in the array will contaminate other image elements. In particular, the finite F ratio of the spectrograph beam produces a characteristic diffraction pattern in the image plane, so that an image from a small source in the object plane extends significantly beyond the size of the original source. Because this happens for all points in the spectra that are produced by the spectrograph, each spectrum is surrounded by a blurred version of itself, with an intensity that drops only slowly with distance.

It is inevitable then that some of this light contributes to neighboring spectra, to a degree that is proportional to the density of spectra on the detector. This can easily be controlled by means of the angle of dispersion relative to the grid of the MLA, but is accompanied by a change in the available spectral range.

The diffraction properties of the instrument can be characterized very well, but the importance of this contamination is not immediately apparent because it can be removed from the data in principle. Moreover, any contribution of one spectrum to another is blurred significantly and is offset in wavelength by an accurately known amount that depends only on geometric factors. This produces a spectral contamination that is much easier to separate from the uncontaminated spectra than the contamination caused by the direct spatial smearing, which is typically found in traditional slit spectrographs.

A theoretical model of this contamination, which assumes that only diffraction contributes significantly, yields an estimate of this contamination of about 2% in the continuum and up to 20% in the cores of the strongest spectral lines, where the intensity of the spectrum can be more than an order of magnitude lower than that in the continuum. The contamination itself can be removed by careful characterization of the instrumental point spread function (PSF), but the increase in the noise level of the data that results from this contamination can only be mitigated by increasing the dispersion angle, although this is only of real significance for the steepest and strongest of spectral lines. It consequently requires a reduction in the spectral range.

2.4. Straylight

In addition to the diffraction-induced redistribution of light, there are other sources of straylight that can be significant, but are much more difficult to model. One obvious such source is the scattering of light on the surface roughness of the microlenses. The main driver for this roughness is the etching process itself, which was used to create the microlenses in the first place. The importance of this scattering is not easily estimated because it can be strongly dependent on the size of the structures. Moreover, we have no knowledge of the structure function of the microlens surface roughness, other than that it is likely proportional to the etching depth, which is at a maximum near the edges.

When we assume that much of the surface structure is at or below the scale of a wavelength, the scattered light is likely to have a wide and homogeneous angular distribution. Therefore, it should be possible to remove some of this contribution from the frontside microlenses by using a mask on the exit side of the MLA. In Sect. 2.2.2, a pupil stop of approximately 70×70 µm near the back side of the MLA was found to be effective in eliminating unwanted diffraction maxima. The distance from the front to the back of the array is approximately 100 times larger than the aperture size of this pupil stop. The removal of light scattered over a wide angle from the frontside of the array is therefore expected to be very effective.

The scattering contribution from the second lens in the MLA, however, has no distance to this mask and therefore cannot be removed in this way. It is accordingly critical that the surface quality of these lenses is as high as possible.

3. MiHI prototype

Because we aim to develop a prototype integral field unit and not an entire instrument, we avoided as additional work and costs as much as possible by executing the prototype as a plug-in for an existing spectrograph. This is the TRIPPEL spectrograph (Kiselman et al. 2011), which is installed at the SST (Scharmer et al. 2003). The properties of this spectrograph provide the starting point for the microlens specifications.

The TRIPPEL spectrograph installed at the SST is a Littrow spectrograph, which has a collimator lens with a diameter of 125 mm and an effective focal length of approximately 1500 mm. Allowing for a 3 mm reduction of the radius for mounting, the pupil size on the grating should not exceed 120 mm, requiring a minimum formal beam F ratio of 12.5 or more. From the optical model of the TRIPPEL spectrograph, the maximum field size over which diffraction-limited performance can be obtained with a fully illuminated grating was found to be about 42×42 mm.

3.1. Microlens array

The prospect of using image restoration on the data imposes requirements on the minimum FOV, which for practical reasons was set to 128 × 128 critically sampling image elements. The maximum area over which the spectrograph can deliver diffraction-limited optical performance is 42×42 mm. This fixed the MLA pitch to approximately 42 mm/128 ≈ 325 µm.

The F ratio of the beam emerging from the MLA is not dependent on the properties of the telescope beam, but is given by Eq. (2) instead. For a beam matching the F ratio of TRIPPEL and a wavelength of 630nm, we have $d = 19.2\,N$, yielding $N = 16.9$ for $d = 325\,\mu$m, thus creating space for $16.9^2 = 286$ spectral resolution elements.

Although the grating is fully illuminated in this configuration, it is also apodized due to diffraction effects. In practice, the illumination pattern of the primary maximum of a diffraction pattern can be fairly well approximated with a 2D Gaussian, which results in a PSF with a full width at half maximum (FWHM) that is approximately twice as large as that of a homogeneously illuminated pupil. Therefore, the diffraction-limited PSF of the spectrograph does not have the formal FWHM of 7.8 µm, but one that is estimated to be closer to 15 µm. This matches the scaled image in $F2$, that is, 325 µm/16.9 = 19.2 µm, fairly well and suggests that we can expect each monochromatic image element imaged by the spectrograph to be a strongly blurred version of the scaled image in $F2$.

We can calculate the dispersion of a Littrow spectrograph with an effective focal length $L_{\rm eff}$ and a grating with a blaze angle of $\theta_{\rm B}$ from

$$\frac{\partial x}{\partial \lambda} \approx \frac{2L_{\rm eff}\tan\theta_{\rm B}}{\lambda}$$

and it is around 1.05 mÅ µm^{-1} in the focal plane for $L_{\rm eff}$ = 1500 mm and $\theta_{\rm B} = 63°$ at a wavelength of 630 nm. A single scaled MLA element of 19.2 µm thus covers a spectral bandwidth of 20.2 mÅ, suggesting that

$$R = \frac{\lambda}{\Delta\lambda} \approx 3.1 \times 10^5,$$

assuming that spectral structure on scales smaller than one MLA element is completely destroyed by smearing. This resolution will only be achieved for a fully illuminated pupil, which may not be the case for at least some image elements due to alignment errors (see also Sect. 2.2.2). The true value of the resolution might therefore differ somewhat, and remains to be determined experimentally.

Although it can be argued successfully that this spectral resolution is much higher than necessary for solar observations and

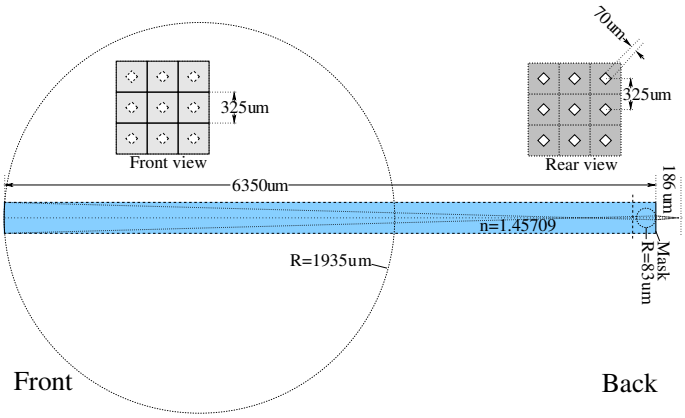

Fig. 5. Cross section of a single element of the double-sided MLA. The blue area show a single micro-optical element out of an array of 128×128. The curved surface with a radius of 1935 µm on the frontside constitutes the first microlens, and the small droplet with a radius of 83 µm on the back forms the second microlens. Inserted are the front view, showing the array layout with 100% fill factor, and the rear view, showing the black chromium mask with integrated apertures.

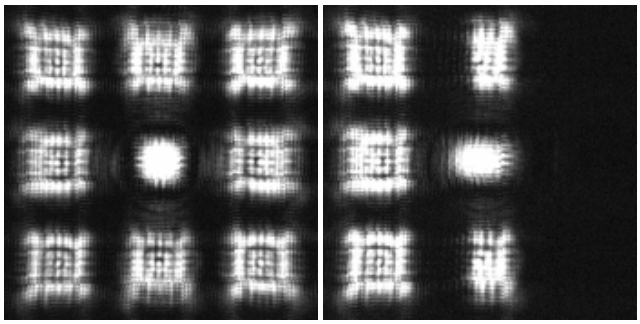

Fig. 6. Image of a diverging beam, sampled by an MLA, imaged at a distance of approximately 30 mm from the focal plane. Only the central microlens has a secondary microlens placed behind it that reimages the micropupil that forms behind each microlens on the camera. *Left panel:* interference pattern that is visible in most subfields is absent in the reimaged micropupil in the center. *Right panel:* as in the *left panel*, but with the right half of the MLA masked. The images of the partially masked microlenses clearly show the mask, but on the left side, consistent with the point reflection that is intrinsic to an image formed by a pinhole. In contrast, the image produced by the secondary microlens is only slightly affected.

that a larger spectral range would be a better way to spend the spectral elements, such a change requires an extensive modification of the spectrograph and cannot be made using the existing instrument. At this resolution, the spectral range of 286 resolution elements still amounts to approximately 5.7 Å, which is large enough to contain a modest number of spectral lines at this wavelength, and for which a high transmission narrowband prefilter can be obtained with relative ease.

Armed with the dimensions and requirements, we are ready to calculate the physical specifications of the MLA. The frontside lenses must be square to achieve the maximum filling factor, but it also must have a fairly large pitch of 325 µm. On the one hand, this imposes limits on the minimum focal length that can be achieved, depending on the technique used to fabricate them. On the other hand, the F ratio of each lens must be kept well below the maximum F ratio imposed by its own diffraction limit.

The second MLA is at least as challenging because the focal length must be rather short to achieve the scale factor, and the pitch must match that of the frontside array. In addition, alignment with the frontside array must be maintained to within a fraction of a micron, or the instrument would become very difficult to calibrate. Finally, because any scattered light from this surface has unimpeded access to the interior of the spectrograph, the surface quality must be as high as possible.

A schematic drawing of a cross section of an MLA element, together with the relevant dimensions, is shown in Figure 5. To solve the alignment problem, the arrays were fabricated on two sides of one substrate, bestowing the manufacturer with a difficult initial alignment problem, but guaranteeing that the alignment, once achieved, is accurately maintained over time. A mask, consisting of black chromium, was applied to the backside of the array, with 70×70 µm apertures, rotated by 45° about the optical axis, in the location of each backside lens. The mask absorbs the light in all diffraction maxima other than the central and second maxima, as well as a large fraction of the scattered light contributions from the frontside of the MLA, preventing it from traveling any farther into the instrument. The backside lenses were created using a reflow technique, which allows the surface of the lens to form under the influence of surface tension, which generates a surface with an extraordinarily low surface roughness.

Real MLA. Upon fabrication of the double-sided MLA, some basic properties were checked in the laboratory to verify the results obtained with the numerical model. An unmasked and uncoated array was first used to verify that the effect of the second MLA was as predicted by the model.

Figure 6 shows the transmission of a spherical monochromatic wave, imaged directly by the camera at a distance of a few millimeters behind the array. The distance is enough to place the sensor well out of focus, near the position where the grating would be in the final instrument, but without resulting in an overlap of the light passing through each image element.

The incoming wavefront is deliberately made divergent, so that only the light passing through one image element on the front side of the array passes through the secondary lens positioned directly behind it. The light from all other frontside image elements does not pass through their corresponding backside lenses, but instead passes through the uncoated flat backside of the substrate. This is clearly visible from the illumination pattern on the sensor, which shows a nearly circular central spot surrounded by blurry squares, modulated by interference fringes on a variety of spatial scales, which roughly resemble the calculated image in $F2$ from Fig. 4.

Partial obstruction of the incoming light by a mask in front of the MLA confirms that the blurry squares are unsharp representations of the lenses on the frontside of the array. The central spot shows a small elongation in the direction of the intensity gradient on the corresponding frontside lens that is similar to the results shown in Fig. 4.

3.2. Optical design

The optical design of the MiHI prototype, shown in Fig. 7, revolves almost entirely around adaptations of the image scale. This is a consequence of making use of an existing spectrograph. The design consists of a primary and a secondary reimager, a context imager, and the MLA.

The primary reimager consists of two lenses, L2 and L3, and is needed to magnify the image in telescope focus from a scale of 0.00456″ µm^{-1} to a scale at which it can be sampled critically

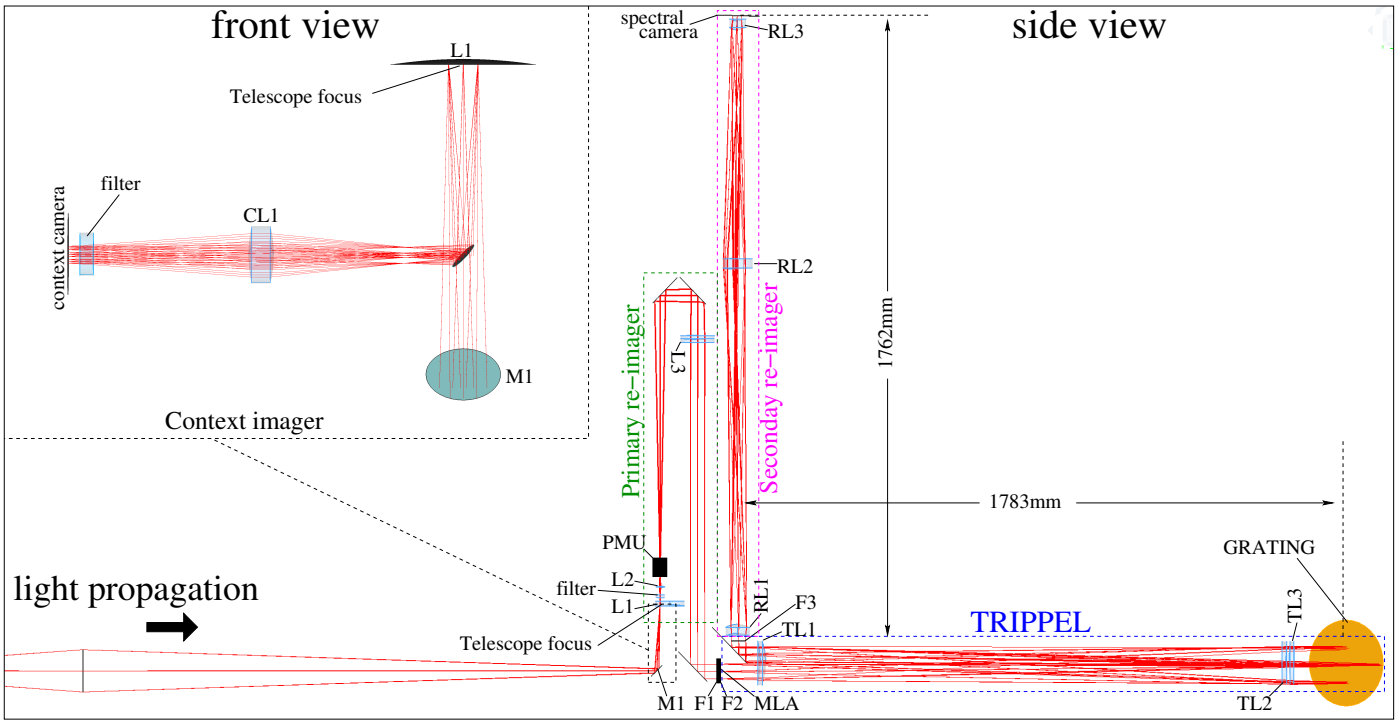

Fig. 7. Optical design of the MiHI prototype. The design consists of a primary reimager, the MLA, the TRIPPEL spectrograph, a secondary reimager, and a context imager that is reflected at a right angle out of the plane of the main figure. The original TRIPPEL spectrograph is the part contained in the dashed blue box. Some dimensions are indicated in the figure for reference purposes.

by the MLA, while simultaneously making the beam sufficiently telecentric for the light to pass through the MLA. At 630 nm, the diffraction limit of 0.13 arcsec must be sampled by 2 pixels, yielding a pixel size of 14.3 µm in science focus. To match this with 325 µm pixels, the pitch of the MLA, a scale factor of 1:22.8 is required, which was accomplished using a combination of an off-the-shelf doublet lens with a focal length of 1000 mm, L3, and a custom-made lens with a focal length of 43.9 mm, L2. The telecentricity of the beam can be controlled using the separation between these two lenses. The focal depth after magnification is so large, however, several meters, that no focus mechanism is required.

If the spectrograph were designed for the camera pixel size, the secondary reimager would not be needed. Unfortunately, that is not the case here, so that it is required here to adjust the scale of the spectrograph output image to the pixel scale of the spectral camera to maximize the FOV of the instrument. The camera pixels of 6.4 µm require a scale change of almost 2:1 while maintaining diffraction-limited performance. Although the size of the field in spectrograph focus is fairly large, at 42×42 mm, the limited space in the room where the instrument needs to fit requires the reimaging optics to be not longer than 2 m. This could only be accomplished using two large field-flattening lenses, RL1 and RL3, and a large aspherical reimaging lens, RL2.

3.2.1. Context imager

The MiHI prototype has a relatively small FOV, so that a context imager is needed to position the instrument sufficiently accurately to target a specific feature on the solar surface. Although important for positioning while observing, the context image is not only useful to place the observations in context, it can also serve as a source of information regarding seeing-induced image degradation.

Because a MiHI instrument has imaging as well as spectral capabilities, the high spectral resolution results in rather low light levels and correspondingly noisy data, so that directly using the instrument data to restore the image information may not be the optimal solution. Specifically, the speed of any cameras large enough to contain the spatio-spectral image is still too low to freeze the seeing completely, causing an inconsistency between a basic assumption underlying the multiframe blind deconvolution (MFBD; van Noort et al. 2005) wavefront-sensing technique and the data. A straightforward solution to this problem can be obtained by running the context imager in sync with the spectral camera, but at an integer multiple of the spectral camera frame rate. This ensures that several independent wavefront estimates can be used to estimate the PSF, each of which is much better determined than would have been the case with the much noisier data from the spectral camera. In addition, while the instrument image is modulated by the polarimetric modulator, the context image is not, so that absolutely no changes are made to the image that is used to sense the PSF. This minimizes the risk of polarization-induced crosstalk.

To ensure that we can use the context imager for this purpose, we must feed some of the light that hits the entrance of the instrument without significantly reducing the light level in the instrument. To this end, an uncoated plano-concave lens (L1) was inserted in the science focal plane and was decentered by approximately 28 mm, thus reflecting approximately 4% of the incoming light back, but at an angle of approximately 10° with respect to the incoming beam direction, so that the incoming and outgoing beam paths can be separated. This lens was then coated with black chromium, except in a small window of 2 × 2 mm that serves as the entrance window of the instrument. The black chromium was tuned to have a reflectivity similar to the uncoated silica of the lens, so that the entrance window is visible in the raw context image, but it can be removed

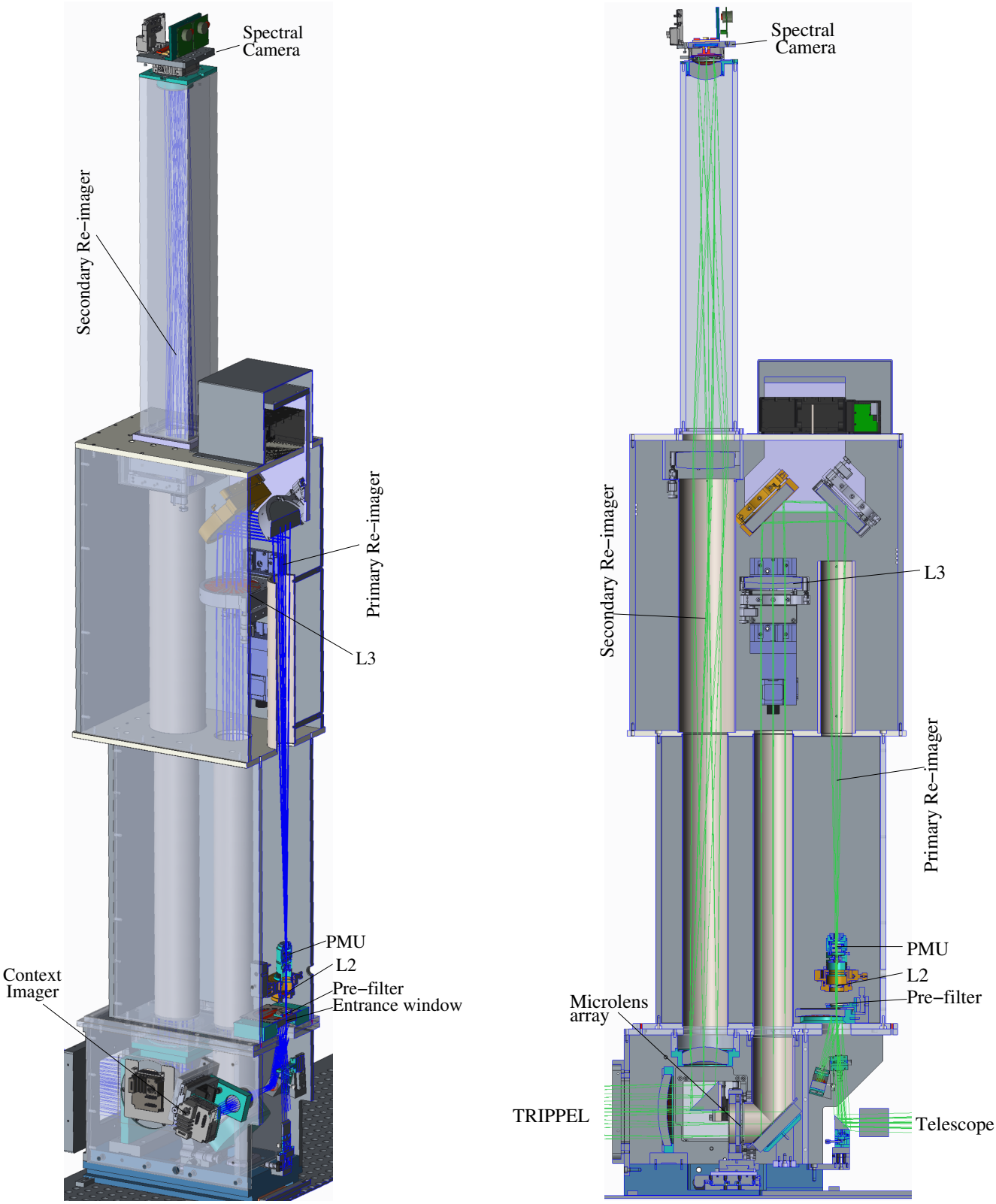

Fig. 8. Mechanical design of the MiHI prototype. *Left panel*: cross section seen from the front side, with the light from the MLA exiting to the spectrograph on the rear. *Right panel*: cross section seen from the side, with the telescope beam entering from the lower right.

by application of a flat-field correction, and does not cause the S/N of the context image to vary much inside and outside the window.

The reflection off the concave surface reimages the pupil at ≈200 mm from the science focal plane, which is then used to reimage the context image onto the context camera while scaling the image appropriately to critically sample the context image with the pixel size of the camera. The entire length of the context imager was kept to only 300 mm. This minimizes the risk of thermally induced image motion.

3.2.2. Polarimetric modulator unit

The polarimetric modulator consists of two ferroelectric liquid crystals (FLC), one with a retardance of $\lambda/2$, and one with a retardance of $\lambda/4$. The two half-inch FLCs were custom made for the target wavelength of 630nm and were AR coated to minimize the loss of light and the risk of interference fringes.

An analyzer linear polarizer was then mounted behind the two FLCs to ensure that the polarimetric modulation does not interact with the remaining part of the instrument. The polarimeter is therefore only single beam, which leads to a 50% loss of light, but it greatly simplifies the secondary reimaging assembly of the instrument.

The polarimetric modulator unit (PMU) was mounted on the lens holder that holds the first lens of the primary reimager (L2 in Fig. 8) in an adjustable housing that allows for a rotation between the first and second FLC, as well as for an arbitrary angle of the analyzer polarizer. The entire modulator unit was fit in a cylinder of 40 mm length with a diameter of only 30 mm, and was placed in the pupil of the primary reimager.

Although this increases the chance of introducing an unwanted image degradation due to optical imperfections of the FLCs, the pupil has a diameter of only 0.8 mm, so that the risk of significant image degradation is low. Moreover, placing the FLC in the pupil ensures that no pupil wobble can be produced, which could cause the instrumental properties to depend on the modulation state.

3.3. Mechanical design

The mechanical design, shown in Fig. 8, follows simple rules of solidity and thermal mass to ensure the most stable environment for the optical components. To allow the plug-in to be inserted into the beam and removed again without compromising the performance of the original TRIPPEL spectrograph, the design has the same footprint as the existing slit box and can be inserted in its place.

The envelope of the plug-in was made from solid aluminum to maximize the thermal conductivity and keep the weight down to an acceptable level. Despite this, the total weight still exceeds the lifting capacity of the average person, which requires the unit to be assembled in four separate pieces.

3.4. Spectral camera

The sensor of the MiHI prototype needs to detect all resolution elements while critically sampling. From the dimensions of the data cube, 128×128×324, a total of 5.3 million independent information elements need to be recorded. For all of them to be critically sampled, that is, by at least 2 pixels in each dimension, a sensor with at least 20 megapixels (Mpx) is required. In addition, the seeing freezing condition favors a frame rate of at least 100 fps, or 2 gigapixels s^{-1}.

These requirements are well outside the range of ordinary CCD sensors and can currently only be obtained using CMOS sensors. Fortunately, large-format CMOS cameras with very favorable frame rates have increasingly become available in recent years. At the time of design, the specifications did not quite meet the demands imposed by the MiHI prototype in speed and size, so that a compromise was needed. The choice was made for a camera based on the CMV20000 sensor by CMOSIS. This 20 Mpx device can run at full speed in snapshot mode at a frame rate of 30 fps. This is fast enough to freeze image motion in moderate to good seeing conditions.

Because it is a sensor with fully parallel readout, it is not a sensor with an intrinsically high readout rate. This results in an impressive rms readout noise of only 8 electrons (e^-). Unfortunately, this number does not tell the whole story, as each of the sensor columns is read out by its own readout register. Although this is not by itself a problem, the variability of each register as a function of light level and thermal conditions is not identical, resulting in artifacts that are visible as vertical stripes in the acquired images. To minimize adverse effects caused by this, the camera selected for the prototype, a Jai Spark SP20000, was equipped with a windowless version of this sensor, which was thermally stabilized to within 0.1°C using a two-stage water-cooled closed-loop thermoelectric temperature-control circuit to avoid time-dependent drifts and interference fringes.

The 1200 MB s^{-1} of data produced by the camera were captured using a small multicore desktop PC, compressed by a factor of 2–3 using a simple lossless bit-slicing algorithm. The data rate then averaged about 550 MB s^{-1}, which is sufficiently low for storage on an external network storage via a 10 Gb fiber link.

For reasons of simplicity and synchronization, the same camera was also used for the context imager, for which the selection of a region of interest (ROI) allowed it to run more than three times faster without losing any of the relevant telescope FOV due to clipping. The cameras for the context imager and the spectral imager were externally triggered, such that three context images were recorded for each exposure of the spectral camera.

4. Results

The MiHI prototype was used in two separate observing campaigns, with a change of a number of parts in between. The first campaign was in October 2016 and was mainly used to set the instrument up, test the optical and spectral performance, and record the first data set, so that the data reduction procedures could be developed. In the second campaign in July 2017, a polarimetric modulator was added, and the context imager field mirror was changed from aluminum to black chromium to reduce the contrast of the imprint of the instrument field stop in the context image, as described in Sect. 3.2.1.

The optical setup consisted of the plug-in described above, mounted on the TRIPPEL spectrograph. The beam from the telescope passed through the SST adaptive optics and tip-tilt correction systems.

The prefilter that was fitted to the instrument was a five-cavity filter, centered at 6302.0 Å, with an FVWM of 4 Å and a ±0.1% transmission bandwidth of 5 Å. The filter had a peak transmission of 85%, so that a reasonable S/N of the spectra could be obtained in an exposure time of only 30 ms. The plug-in was used in two configurations: with the prefilter just behind the instrument entrance field stop, combined with a separate filter for the context imager, and with the filter positioned before the entrance window, so that it could be shared between the instrument and the context imager. The data were used to evaluate the basic properties of the MiHI prototype.

4.1. Imaging properties

The imaging performance of the plug-in on the TRIPPEL spectrograph was first evaluated using a specifically designed side-port mount. This allowed the direct image from the spectrograph to be observed with a camera.

Because the beam is not demagnified, the focal plane is somewhat oversampled, so that all frequencies in the image can

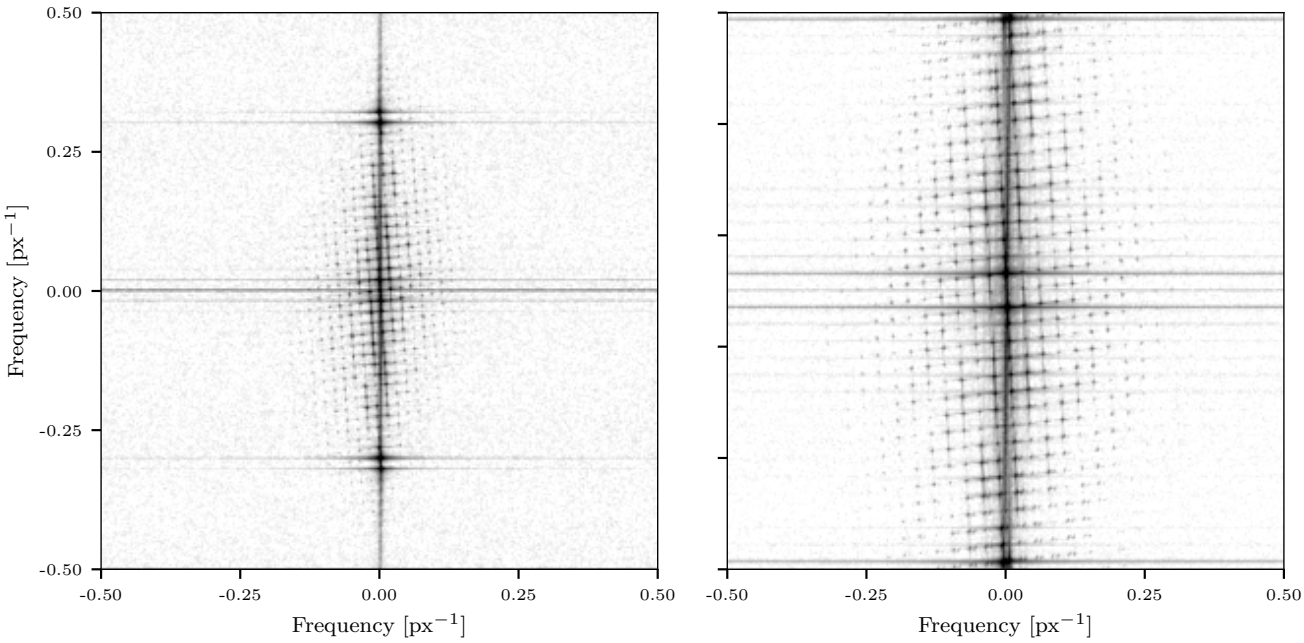

Fig. 9. Power spectrum of a MiHI frame before demagnification (*left*) and after demagnification (*right*). The periodic character of the image is clearly visible as regions of enhanced power that do not extend outside of the frequency domain for the image recorded before demagnification, indicating the image is critically sampled, but that clearly extend outside the frequency domain for the demagnified image, indicating the image plane is undersampled.

be clearly seen in the power spectrum. This is shown in Fig. 9. Clearly, the image frequencies are mainly concentrated in the vertical direction, which is the direction in which the spectra are stacked above each other. The horizontal direction, however, in which the spectra are dispersed, does not show significant power above a frequency of ~0.2 px^{-1}, some 30% of the Nyquist frequency. This indicates that this dimension is significantly oversampled.

We are not particularly interested in sampling the image information introduced by the MLA critically. The camera was therefore mounted behind the secondary reimager, which increased the image scale by a factor 1.8. The power spectrum of a low-contrast image, shown in Fig. 9, indicates that the spectral direction is still somewhat oversampled. In the vertical direction, however, the image is now slightly undersampled. This compromise comes at no significant cost because although the undersampled frequencies will be aliased to lower frequencies, the pattern they produce is attached to the MLA, is thus fixed in time, and can be removed by traditional flat-fielding.

4.2. Instrument transmission

The quality of the MLA is not predominantly determined by the surface accuracy of the microlenses, but is dominated by the alignment accuracy of the front- and the backside lenses in each of the microlens systems. A significant error in the alignment results in a displacement of the pupil on the grating. When this is large enough, it will cause a fraction of the transmitted light to miss the grating entirely.

Figure 10 shows a featureless image that was observed with the spectral camera. It was produced by averaging a large number of individual frames that were recorded at random positions on the solar disk. The image shows a clear left-right asymmetry that is caused by the nonuniform camera response, and few individual spectra that are clearly dimmer than the majority. These are visible as dark streaks in the image. The majority of these dark spectra are easily confirmed to be associated with individual misalignments because tilting the MLA causes them to brighten as the vast majority of the other spectra darken.

Nonetheless, most of the dark spectra still contain some light, as can be confirmed by the presence of spectral signatures in the expected locations. Only two or three of the dark spectra were found to transmit an undetectable amount of light. Even when we demanded relatively high uniformity and only defined an element as good when the transmission exceeded 30% of the average, the defect rate of the array was still only about 0.1%.

To estimate the transmission properties of the instrument, the averages of the spectral and context images were compared. The integrated total amount of charge on the spectral camera was compared to the total amount of charge on the context imager, averaged over a representative number of pixels. This was taken to equal the number of image elements covered by the spectral camera. The difficulty of using this method lies in the brightness of the context image, which required the use of a strong neutral density (ND) filter to avoid saturating the sensor. This made it necessary to measure the attenuation factor of the ND filter, which was found to be around 0.001. This value is already challenging to measure with the limited dynamic range of a 10 bit camera. Therefore, the determination of the instrument transmission is probably not particularly accurate.

The overall transmission of the instrument was found to be approximately 25% without the polarimetric modulator and about 20% with the polarimetric modulator in dual-beam mode. These numbers agree reasonably well with a surface-by-surface calculation, using ROM estimates for the losses incurred on each surface.

As a sanity check, the photon flux on the context imager was calculated based on a model of the solar flux, the Earth's atmosphere, telescope transmission, instrument transmission, and quantum efficiency. The best estimate for all these numbers yields a detected charge per pixel per exposure of 33 ms of 21.7 ke$^-$, which agrees reasonably well with the 15.1 ke$^-$ that

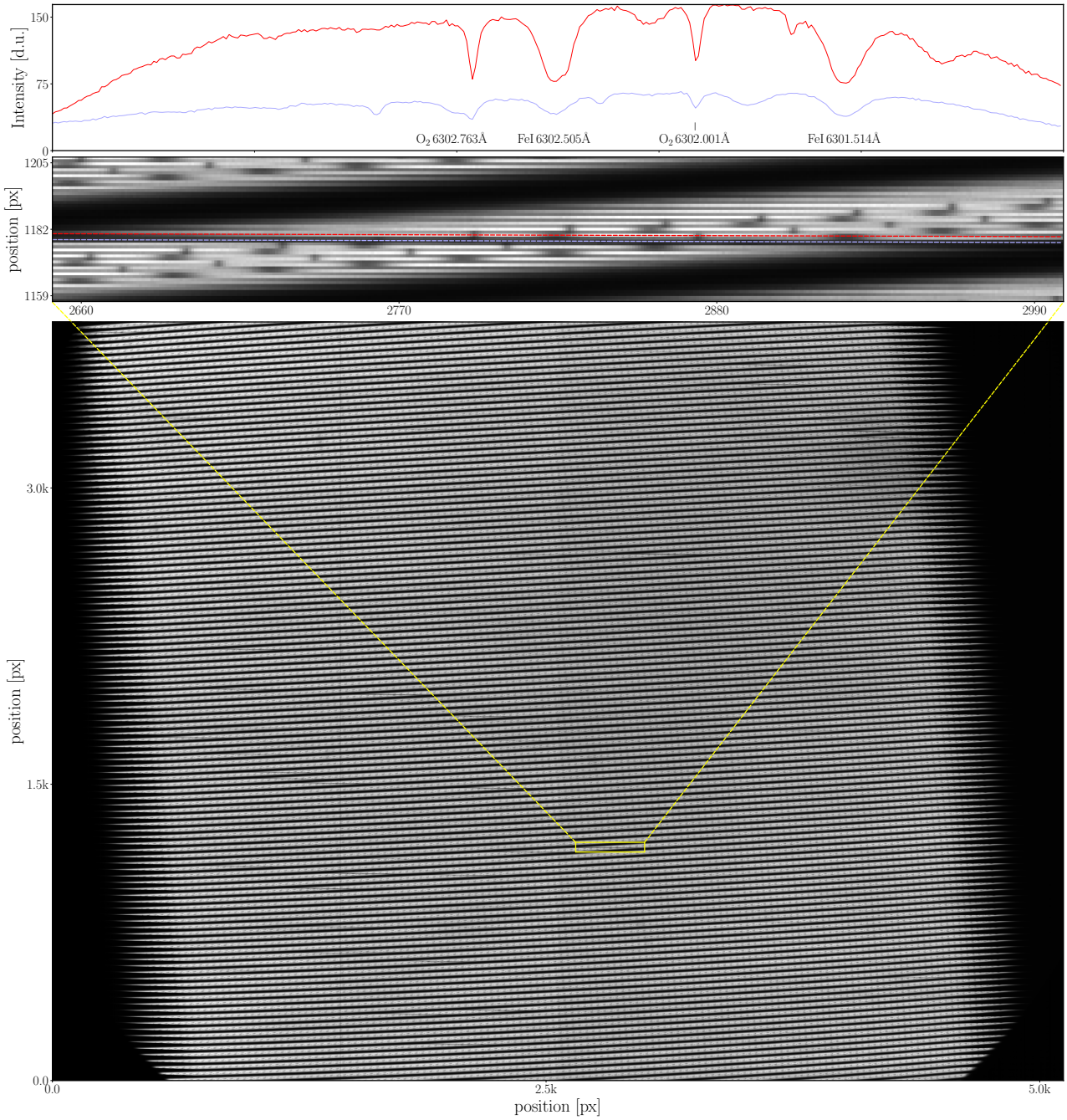

Fig. 10. Example of a dark-corrected MiHI data frame of a featureless solar scene. Clearly, the image recorded by the sensor, shown in the *bottom panel*, is far from featureless and is dominated by spatial structure introduced by the MLA and by spectral features from the solar spectrum. These features are more clearly visible in the *middle panel*, where the broader dark features are the solar absorption lines, and the narrow features are due to absorption by O_2 molecules in the Earth's atmosphere. The wavelength direction is approximately horizontal throughout the image, but varies somewhat due to image distortion. The measured signal level along the dashed red and blue lines in the *middle panel* is plotted in the *top panel*, together with an indication of two telluric O_2 lines and two solar Fe I lines that are present in the spectral band. The red line traces the spectrum of a single MLA element with typical transmission properties, and the dark area traced by the blue line contains the spectrum of a misaligned low-transmission MLA element. Clearly, the signal in the dark area still contains some spectral information of the corresponding MLA. The broad dark slanted bands are the prefilter taper areas between two image rows.

were actually detected. This places the best estimate of the overall transmission of telescope and instrument at approximately 4%.

4.3. Spectral resolution

Data with high spatial resolution are routinely acquired using filtergraph-based instruments. Therefore, the spectral performance is clearly the aspect of this type of instrument that sets it apart from existing solar instrumentation. Establishing the spectral resolution of solar spectroscopic instruments is traditionally accomplished by minimizing the difference between an average spectrum of the Sun at disk center with the convolution of a high-resolution standard solar spectrum, convolved with the spectral PSF. This fit must be carried out together with an estimate of the gray straylight (the

wavelength-independent or undispersed scattered light from within the instrument).

However, this method cannot be used directly for the MiHI prototype because it requires the extraction of the spectra from the raw data. This nontrivial task was described in van Noort & Chanumolu (2022) and van Noort & Doerr (2022). Moreover, most of the straylight present in the data is not really straylight at all, but is produced by the wings of the instrumental PSF, which cause the individual spectra to contaminate the adjacent spectra. This contamination is inevitable, but it is not gray because it contains spectral information, albeit at a lower spectral resolution. Although this effect might be addressed by careful deconvolution of the data, this effort requires knowledge of the instrumental PSF, which varies across the image plane. This is the topic of van Noort & Chanumolu (2022).

Fortunately, the MiHI prototype allows for the spectral resolution to be determined in a different way: by assessing the imaging performance of the instrument in the direction perpendicular to the spectral direction. For reasons of symmetry, the optical performance is not expected to be very different in the direction of dispersion from that in the direction perpendicular to the dispersion, so that the latter should give us a reliable estimate of the spectral performance even when no high-resolution features are present in the spectra.

From Fig. 9, we estimate that the unscaled image is slightly oversampled because no significant power appears to be present above $k_y = \pm 0.35\,\mathrm{px}^{-1}$, or approximately 70% of the vertical sampling resolution limit. We can translate this into a spectral resolution by measuring the distance in pixels between two points in the spectra with known wavelengths. The centers of two well-known telluric O_2 lines, with wavelengths of 6302.001 and 6299.231 Å, respectively, were measured to be spaced 448 pixels apart. This yields a spectral pixel size of 6.2 mÅ, with a corresponding spectral sampling resolution limit of 12.4 mÅ. The highest frequencies in the image are only 70% of this value, therefore the spectral resolution is estimated to be 12.4/0.7=17.7 mÅ, or $R = 3.5 \times 10^5$, which agrees reasonably well with the theoretically calculated value of $R = 3.1 \times 10^5$ that is expected from Sect. 3.1. When we assume that the optical performance of the reimaging optics is close to diffraction limited, this resolution is retained in the demagnified spectral image, although we slightly undersample it there.

We recall that this is a representative number only, and that the spectral resolution is inevitably variable across the FOV. This is largely due to the correspondence of the field position to an angle in the pupil, which adds up to the grating angle to determine the dispersion. In combination with a field dependence of the optical performance and some geometric image distortion, this causes the spectral resolution to vary across the FOV. The spectral resolution of each pixel in the FOV is therefore best determined by using a detailed full model of the entire instrument.

4.4. Spatial resolution

Because the frequency content of the spectral images is not dominated by spatial frequencies, but by artificially induced frequencies from the MLA, it is not meaningful to determine the spatial resolution by looking at the power spectrum of the images. The intrinsic imaging properties of the instrument were therefore determined directly from imaging a pinhole, kept in focus by the adaptive optics system. The small number of pixels with a significant light level makes it easy to measure the vertical extent of the pinhole, as we show in Fig. 11, and can be readily confirmed to have a similar extent as in the context image. The extent in the horizontal direction can be determined by counting the number of occurrences of the same spectral signature along the central band of spectra. In this case, about seven repeats of the same spectral signature can be counted, which is roughly in agreement with the eight bands counted in the vertical direction. It is also compatible with the image recorded with the context imager.

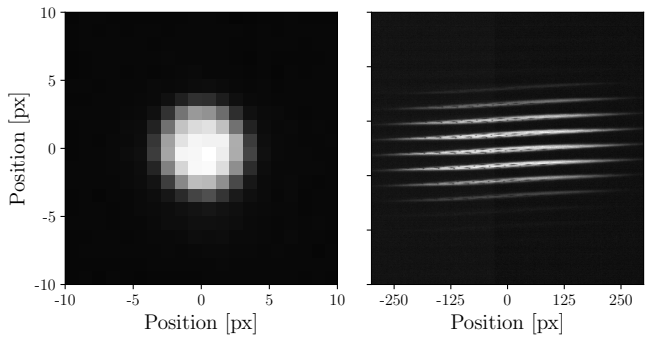

Fig. 11. Image of a pinhole, as seen by the context imager (*left*) and the MiHI spectral camera (*right*).

A thorough and more complete assessment of the image quality of the instrument requires the extraction and restoration of high-quality solar data. We refer to van Noort & Doerr (2022) for this.

4.5. Straylight

In the determination of the straylight properties of the instrument, the limited FOV and high contrast are particularly helpful. Although there is cross-contamination of the spectra to each other due to diffraction effects and optical imperfections, this is not straylight in the classical sense because the mapping of that light from its source is known. It can in principle be corrected for by deconvolving the data.

The classical wavelength-independent (gray) straylight that usually produces an offset on long-slit spectra, can be measured independently from the spectra in the dark regions of the image, far away from any direct illumination. Figure 12 shows a region in the lower right corner of the spectral image, showing three different levels of illumination. By comparing the histograms of the light levels in the spectral box (blue) and the dark areas surrounding the spectra (green), the straylight level can be readily determined. The mean level of the straylight is about 2 counts, which, depending on the wavelength, amounts to between 1.4% of the signal level in the continuum and 5% of the signal level in the core of the Fe I lines. From the red box, which is positioned in an area that is vignetted close to the focal plane of the spectrograph, we can infer that approximately half of the straylight originates in the spectrograph itself, and the other half is produced inside the reimaging optics of the secondary reimager.

The large contribution of the secondary reimager to the total straylight level is not completely unexpected because it contains a large-aperture aspherical lens, with a significant surface roughness at intermediate spatial frequencies, far away from focus. This problem can, however, be easily avoided in a newly built instrument by adjusting the spectrograph properties to the pixel size of the detector that is used. Although additional spatial straylight is likely to be present in the beam already before entering the instrument, its magnitude cannot be measured in this way.

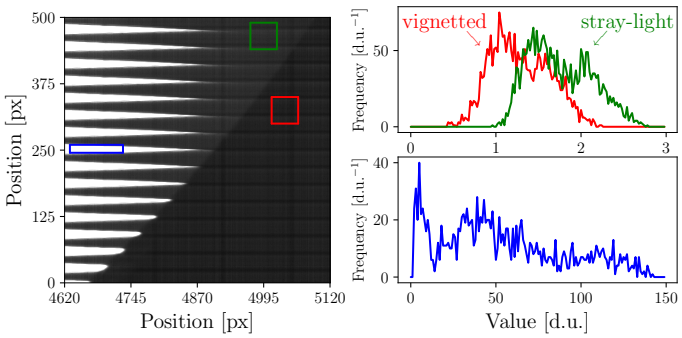

Fig. 12. Assessment of instrumental straylight properties. *Left panel:* saturated image of the lower right corner of the spectral image. Boxes show the vignetted (red), straylight-dominated (green), and signal-dominated (blue) regions. *Right panels:* histograms of these regions with their respective mean values. For the box containing the spectra, the various contributions can be identified as partially overlapping populations, as indicated in the figure.

5. Summary

A prototype microlens-based integral field spectrograph was designed, built, and tested to evaluate the suitability of such an instrument for high resolution solar observations. Diffraction modeling showed that a key element required for reliable high spectral resolution was the use of a two-lens micro-optical reimager within each spatial resolution element that can maintain coalignment with very high accuracy. This was accomplished by manufacturing the two lenses on the front- and backside of a single sheet of silica. The accuracy of the manufacturing methods was sufficiently high to produce an array whose fraction of fully functional reimagers exceeded 99.9%. The optical properties of the array were verified in laboratory experiments and showed good quantitative and qualitative agreement with the properties predicted by numerical modeling.

The plug-in, assembled and mounted on the TRIPPEL spectrograph at the SST, showed close to nominal performance, with a spectral resolution in excess of 3.5×10^5. The instrument transmission was estimated to be between 20 and 25%, which agrees well with a surface-by-surface transmission estimate.

The straylight properties of the instrument itself were found to be typical for spectrographic instruments. They are mostly affected by the quality and number of surfaces needed in the secondary reimager. This can likely be improved significantly by designing a follow-up instrument specifically for a given detector pixel size, thus eliminating the need for any kind of reimaging of the spectrograph focal plane. The majority of the straylight, however, comes in the form of spectral cross-contamination and can only be addressed by careful characterization of the instrumental PSF.

The characterization, reduction, and restoration of the data from this instrument is highly non-trivial. It was presented in van Noort & Chanumolu (2022) and van Noort & Doerr (2022), along with several data sets recorded at the SST in 2017 and 2018.

Acknowledgements. This research has made use of NASA's Astrophysics Data System. This project was supported by the European Commission's FP7 Capacities Program under the grant agreements nos. 212482 and 312495. It was also supported by the European Union's Horizon 2020 research and innovation program under the grant agreements nos. 653982 and 824135. This project has received funding from the European Research Council (ERC) under the European Union's Horizon 2020 research and innovation program (grant agreement no. 695075) and has been supported by the BK21 plus program through the National Research Foundation (NRF) funded by the Ministry of Education of Korea. The Swedish 1 m Solar Telescope is operated on the island of La Palma by the Institute for Solar Physics of Stockholm University in the Spanish Observatorio del Roque de los Muchachos of the Instituto de Astrofísica de Canarias. The Institute for Solar Physics was supported by a grant for research infrastructures of national importance from the Swedish Research Council (registration number 2017-00625).

References

Antichi, J., Dohlen, K., Gratton, R. G., et al. 2009, ApJ, 695, 1042
Bacon, R., Adam, G., Baranne, A., et al. 1995, A&AS, 113, 347
Bacon, R., Copin, Y., Monnet, G., et al. 2001, MNRAS, 326, 23
Beckers, J. M., Dickson, L., & Joyce, R. S. 1975, Appl. Opt., 14, 2061
Beuzit, J. L., Vigan, A., Mouillet, D., et al. 2019, A&A, 631, A155
Cao, W., Goode, P. R., Ahn, K., et al. 2012, ASP Conf. Ser., 463, 291
Cavallini, F. 2006, Sol. Phys., 236, 415
Chae, J., Park, H.-M., Ahn, K., et al. 2013, Sol. Phys., 288, 1
Collados, M., López, R., Páez, E., et al. 2012, Astron. Nachr., 333, 872
Dominguez-Tagle, C., Collados, M., Esteves, M. A., et al. 2018, SPIE Conf. Ser., 10702, 107022I
Groff, T. D., Kasdin, N. J., Limbach, M. A., et al. 2014, SPIE Conf. Ser., 9147, 91471W
Henault, F., Bacon, R., Bonneville, C., et al. 2003, in Proc. SPIE, 4841, 1096
Hinode Review Team, Al-Janabi, K., Antolin, P., et al. 2019, Publications of the Astronomical Society of Japan, 71, R1
Huygens, C. 1690, Traite de la Lumiere (Pierre van der Aa, marchand libraire, A Leiden)
Kentischer, T. J., Schmidt, W., Sigwarth, M., & Uexkuell, M. V. 1998, A&A, 340, 569
Kiselman, D., Pereira, T. M. D., Gustafsson, B., et al. 2011, A&A, 535, A14
Kosugi, T., Matsuzaki, K., Sakao, T., et al. 2007, Sol. Phys., 243, 3
Larkin, J., Barczys, M., Krabbe, A., et al. 2006, New A Rev., 50, 362
Lin, H. 2012, in Proc. SPIE, 8446, 84461D
Lites, B. W., Elmore, D. F., Streander, K. V., et al. 2001, SPIE Conf. Ser., 4498, 73
Macintosh, B., Graham, J., Palmer, D., et al. 2006, SPIE Conf. Ser., 6272, 62720L
Mein, P., & Blondel, M. 1972, Sol. Phys., 27, 489
Nyquist, H. 1928, Trans. Am. Inst. Electr. Eng., 47, 617
Puschmann, K. G., Denker, C., Kneer, F., et al. 2012, Astron. Nachr., 333, 880
Qu, Z. Q., Dun, G. T., Chang, L., et al. 2017, Sol. Phys., 292, 37
Schad, T., Lin, H., Ichimoto, K., & Katsukawa, Y. 2014, SPIE Conf. Ser., 9147, 91476E
Scharmer, G. B. 2006, A&A, 447, 1111
Scharmer, G. 2017, in SOLARNET IV: The Physics of the Sun from the Interior to the Outer Atmosphere, 85
Scharmer, G. B., Bjelksjo, K., Korhonen, T. K., Lindberg, B., & Petterson, B. 2003, SPIE Conf. Ser., 4853, 341
Shannon, C. E. 1949, IEEE Proc., 37, 10
Shimizu, T. 2004, ASP Conf. Ser., 325, 3
Suematsu, Y., Imai, H., Yoshimura, K., et al. 1999, ASP Conf. Ser., 183, 303
Suematsu, Y., Koyama, M., Sukegawa, T., et al. 2017, SPIE Conf. Ser., 10563, 105634M
Tecza, M., Thatte, N. A., Eisenhauer, F., et al. 2000, SPIE Conf. Ser., 4008, 1344
Title, A., & Rosenberg, W. A. 1981, Opt. Eng., 20, 815
van Noort, M., & Chanumolu, A. 2022, A&A, 668, A150
van Noort, M., & Doerr, H.-P. 2022, A&A, 668, A151
van Noort, M., Rouppe van der Voort, L., & Löfdahl, M. G. 2005, Sol. Phys., 228, 191